PCCP

ROYAL SOCIETY OF CHEMISTRY

PAPER

View Article Online
View Journal | View Issue

Cite this: *Phys. Chem. Chem. Phys.*, 2025, **27**, 24641

Photophysical divergence driven by π-spacer variations in the anthracene–cyanostilbene architecture

Cherumannil Femina, [a] Norifumi Yamamoto, [b] Nelliyulla Kappumchalil Ramya, [a] Pookkottu K. Sajith *[a] and Reji Thomas *[a]

Received 8th August 2025,
Accepted 21st October 2025

DOI: 10.1039/d5cp03033a

rsc.li/pccp

A series of four anthracene-incorporated cyanostilbene derivatives with donor–π–acceptor (D–π–A) architectures was synthesized to investigate the effect of a phenyl π-spacer. Compounds without the spacer (**2a**, **2b**) showed low quantum yields (Φ_F = 0.05–0.25) in various solvents, negative solvatochromism, aggregation-induced enhanced emission (AIEE), and red-shifted mechanofluorochromism. In contrast, those with the spacer (**3a**, **3b**) exhibited high quantum yields (Φ_F = 0.75–0.85), positive solvatochromism, aggregation-induced emission (AIE), and blue-shifted mechanofluorochromism, highlighting the key role of the spacer in modulating photophysical properties. Quantum chemical calculations reveal that the compounds incorporating a phenyl π-spacer exhibit conformational flexibility between *syn*- and *anti*-conformers in both the ground and excited states, due to an energetically more accessible transition state relative to analogues lacking the spacer. The findings in this study underscore the importance of strategic structural engineering in anthracene-based cyanostilbene systems, which profoundly influences their photophysical properties, paving the way for their potential use in future optoelectronic applications.

Introduction

Tuning of the photophysical characteristics of organic luminescent materials under ambient conditions is an area of fundamental research and is extensively applied in the field of optoelectronics.[1–5] The conventional π-conjugated compounds without any functional modifications have simple photophysical properties with respect to their structural and functional moieties. Taking this into account, it is necessary to acquire more specific optoelectronic performances, which can be achieved by designing and constructing smart molecules in which the photophysical properties can be tuned in a controlled manner.[6] Therefore, novel molecular designs with tunable photophysical properties can serve as promising candidates for the development of versatile optoelectronic devices.[7–11] The construction and design of such smart molecular structures possessing stimuli-responsive fluorescence switching, such as mechanochromism, thermochromism, vapochromism *etc.*, has received unprecedented attention.[12–16]

Organic luminogens, which are made up of molecules containing electron donor (D) and electron acceptor (A) units, have drawn considerable recognition due to their effectiveness in obtaining emissive compounds owing to their push–pull intramolecular electronic behaviour. Such systems have a wide range of applications in the fields of sensors, fluorescent probes, organic solar cells, and hybrid materials, *etc.*[17–22] The donor (D) and the acceptor (A) units are linked through π-conjugated spacers, creating an efficient path for the transport of charge carriers from the donor to the acceptor by the intramolecular charge transfer (ICT) mechanism. ICT systems based on cyanostilbenes as acceptor units have been widely explored over the past decades and employed as fluorescent probes to indicate the micro-environmental changes.[23–26] Most of the studies in these classes of molecules focused on the proper management and utilization of the phenomena for achieving bioimaging, energy harvesting and display applications. The π-conjugated structures endow ample aggregation modes in the solid state, leading to enhanced solid-state emission, while the ICT phenomenon enhances the emission properties of these molecules in solution. Therefore, the design and synthesis of donor–acceptor-based molecules opens great promise to afford bright emissive materials with tunability in solution and the solid state.[25]

Among various π-conjugated materials, cyanostilbene-based organic fluorophores have drawn interest due to their extraordinary emissive properties resulting from their rigid and

[a] *Department of Chemistry, Farook College (Autonomous), Research Centre of University of Calicut, Kozhikode 673632, Kerala, India. E-mail: femi.fana@gmail.com, norifumi.yamamoto@it-chiba.ac.jp, ramyank2012@gmail.com, pksajith@farookcollege.ac.in, pksajisiv@gmail.com, reji@farookcollege.ac.in*

[b] *Department of Applied Chemistry, Faculty of Engineering, Chiba Institute of Technology, 2-17-1, Tsudanuma, Narashino, Chiba 275-0016, Japan*

twisted geometry along with their tendency to form emissive aggregates in the solid state. Recent reports have shown that the cyanostilbene derivatives with alkyl chains provide flexible solid-state structures with precise control over molecular packing and aggregation, wherein various external stimuli such as heat, light, pressure, *etc.* have resulted in tunable optoelectronic properties.[27–30] Various attempts have been made by supramolecular chemists to design and synthesize molecular systems with multi–stimuli responsive emission switching.[31,32] In this regard, some of the researchers have focused on constructing molecular systems capable of mechanofluorochromism (MFC) properties, which have significant importance in the development of smart devices with potential in the field of sensing and imaging.[33,34]

There are several notable examples of cyanostyryl-based donor–acceptor systems with triphenylamine,[35] carbazole,[33] fluorene[36] and perylene as donors showing multi–stimuli responsive photoluminescence properties. However, cyanostyryl systems incorporating anthracene,[37,38] a well-known chromophore with excellent photophysical properties, as the donor moiety remain relatively scarce in the literature. In our previous study, we reported the ICT and multi–stimuli responsive emission behaviour of alkyl chain variants in a symmetrically modified anthracene–dicyanostyryl D–π–A system, where the donor and acceptor units are separated by a phenyl spacer.[23] Building on these findings, the present work investigates the influence of the π-spacer on the intramolecular charge transfer properties of their homologues (see Fig. 1, **3a** and **3b**) in comparison to their molecular counterpart where the anthracene moiety is directly linked to the cyanostyryl acceptor unit (see Fig. 1, **2a** and **2b**). This study aims to compare the role of donor–acceptor linkages in these molecules in spite of enhanced conjugation in the molecular system with an additional phenyl ring. The intrinsic properties of the core chromophore, independent of alkyl chain variations, are represented by compound **2** (comprising **2a** and **2b**) and compound **3** (comprising **3a** and **3b**). The present study reports contrasting photophysical behaviour of two series of compounds, including the rarely observed negative solvatochromism in compound **2**. Both the compounds showed aggregation induced emission and mechanofluorochromism in the solid state. Herein, we investigated the structural origin of the photophysical divergence of the compounds supported by structural data obtained from X-ray diffraction and TD-DFT calculations.

Experimental and computational methods

All the chemicals and reagents required for the synthesis of anthracene–cyanostilbene derivatives (**2a** to **3b**) were purchased from commercial suppliers and used without further purification. All of the compounds were synthesized by following the reported procedures with modifications and the synthesized compounds were characterized using ^{1}H NMR and ^{13}C NMR spectroscopy in $CDCl_3$ with TMS as an internal standard (see Fig. S1–S6). Compounds **2b** and **3b** were further characterized using single-crystal X-ray diffraction. The single crystals of compounds **2b** (orange-yellow crystal) and **3b** (green crystal) were grown by slow evaporation at room temperature from the respective dichloromethane and ethyl acetate solutions. Fig. S7 shows the ORTEP of compounds **2b** and **3b** drawn at 50% probability. The mass spectral data were obtained from electron spray ionization mass spectroscopy (ESI-MS), model-micromass QTof MicroTM and a Maxis Impact. UV-visible spectroscopic studies were carried out on a Cary 5000 high-performance UV-Vis-NIR spectrophotometer with superb photometric performance in the 175–3300 nm range. The fluorescence lifetime and the steady state fluorescence studies were conducted on an FLS1000-xS-t fluorescence lifetime spectrometer and on an Edinburgh FLS-1000 photoluminescence spectrometer attached with an integrating sphere. All the fluorescence spectra were recorded with a quartz cuvette of path length 1 cm at a slit width of 1 nm. Absolute fluorescence

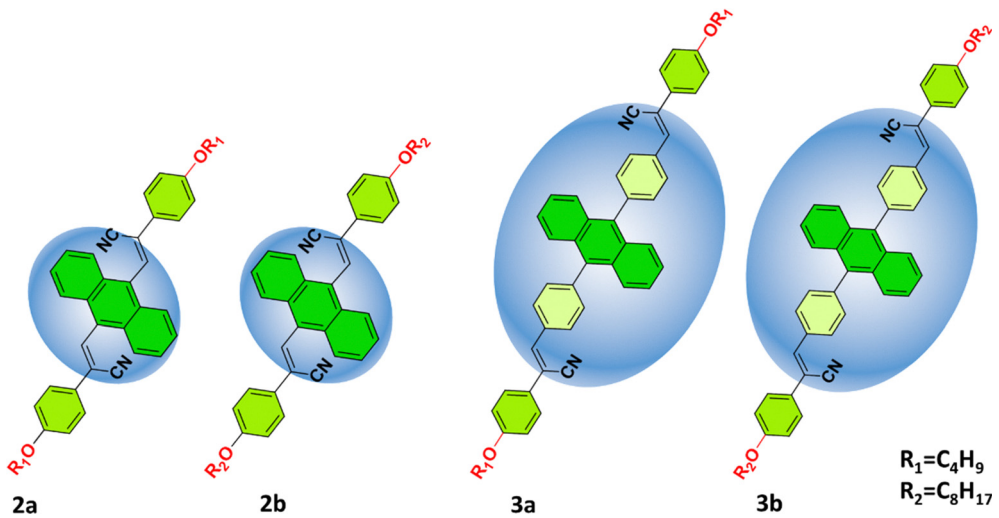

Fig. 1 Chemical structure of compounds **2a–b** and **3a–b**.

quantum yield of the compounds in both solid and solution states was recorded on an LQE-100 LED photo-luminescence quantum yield measurement system. The single crystal X-ray diffraction data were measured on a Bruker AXS Kappa Apex2 diffractometer. The powder X-ray diffraction intensities were measured on a Panalytical Aeris Research diffractometer.

All quantum chemical calculations were performed using the Gaussian 16, Revision C.02 program package.[39] The geometries of the ground state (S_0) and the first singlet excited state (S_1) were fully optimized in the gas phase using density functional theory (DFT) and its time-dependent extension (TD-DFT), respectively. The long-range corrected ωB97-XD functional was employed in conjunction with the 6-311+G(d) basis set for all atoms. Frequency calculations were subsequently carried out at the same level of theory to verify that each optimized structure was a true energy minimum, characterized by the absence of imaginary frequencies. The Gibbs free energies (ΔG) of these conformers were computed at 298.15 K and 1 atm based on the results of the frequency analyses under the harmonic oscillator approximation. The transition state (TS) structures connecting the *syn* and *anti*-conformers were also located and were confirmed to be first-order saddle points by the presence of a single imaginary frequency corresponding to the isomerization coordinate. Vertical absorption energies ($S_0 \rightarrow S_1$) and their corresponding wavelengths were calculated by performing TD-DFT calculations on the S_0-Min geometries. To simulate the fluorescence process, the geometries of the first singlet excited state (S_1) were optimized for all conformers. Emission wavelengths ($S_1 \rightarrow S_0$) were then determined by computing the vertical transition energies from these S_1-Min structures.

Results and discussion

Solution state photophysical properties

In order to explore the role of extended conjugation and alkyl chain variation on the solution state photophysical properties of the newly synthesized anthracene–cyanostyrene derivatives **2** and **3**, we investigated the photophysical properties of these compounds from their dilute solutions in THF (1 μM) (Fig. 2). The UV-visible absorption spectra of compounds **3a** and **3b** showed comparable absorption spectra with maxima centered around 397 nm with shoulder bands centered at 378 nm and 342 nm, respectively. The compounds **2a** and **2b** also exhibited similar absorption spectra with maxima centered at 409 nm (see Table 1). The emission spectra were recorded from the respective THF solution at room temperature and upon 370 nm excitation, **2a** and **2b** exhibited emission bands at 415 and 431 and a major charge transfer (CT) band at 545 nm. In homologues **3**, the emission spectra showed a single band at 485 nm with high quantum yield values (Φ_F) of 0.87 and 0.82, respectively. Conversely, compound **2** showed moderate Φ_F of around 0.05. This enhancement in Φ_F and life-time values (Table 1) is ascribed to the incorporation of the spacer group phenyl ring, which facilitates enhanced ICT compared to **2a** and **2b**.

Solvatochromism

To examine how D–π–A features and solvent polarity influence the photoluminescence, we recorded the emission spectra of compounds **2** and **3** in solvents ranging from hexane to DMF. Fig. 3(a) and (b) show the photoluminescence spectra recorded for the compounds **2a** and **2b** in solvents with varying polarity from hexane to DMF. The photoluminescence spectra of these compounds in all the solvents showed three distinct emission bands. The high-energy minor shoulder peaks observed at 415 and 431 nm appear consistently, irrespective of the solvent used.

Conversely, the band corresponding to the CT state showed a blue shift (584 nm to 524 nm) on increasing solvent polarity from hexane to DMF. The observed negative solvatochromic shift in **2** implies that the dipole moment in the excited state is lower compared to the corresponding ground state. In contrast, the emission spectra recorded for the compound **3** (see Fig. 3(c) and (d)) for solvents of varying polarity showed a single band corresponding to ICT. The single emission band ranging from 460 nm (in hexane) to 535 nm (in DMF), along with reduced intensity on increasing solvent polarity, clearly indicates that

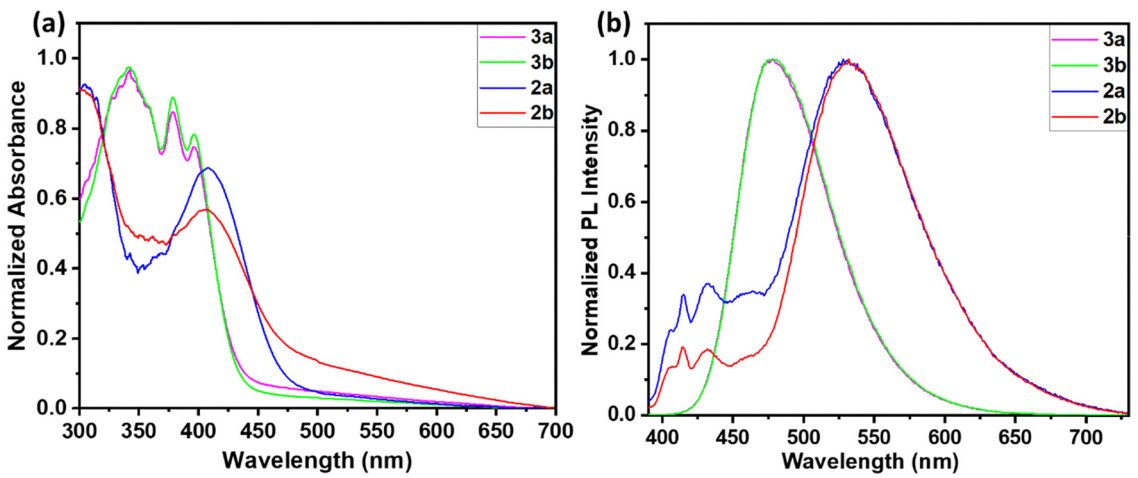

Fig. 2 Normalized (a) UV-visible absorption and (b) emission spectra of the compounds **2a-3b** recorded from THF solutions (1 μM), λ_{ex} = 370 nm.

Table 1 Absorption maximum, photoluminescence maximum, and fluorescence quantum yield of the compounds recorded in THF solvent

Compounds	λ_{abs} (nm)	λ_{em} (nm)	τ (ns)	Φ_F
2a	408	545	1.22	0.05
2b	409	553	0.75	0.06
3a	342, 379, 397	485	2.72	0.87
3b	343, 378, 398	485	2.68	0.82

Table 2 Photophysical parameters of compounds **2** and **3** in different solvents of varying polarity

Compound	Solvent	λ_{abs} (nm)	λ_{em} (nm)	τ (ns)	Φ_F	k_r	k_{nr}
2a	Hexane	407	584	2.57	0.24	0.09	0.296
	Toluene	408	560	1.53	0.17	0.11	0.542
	THF	408	545	1.22	0.05	0.04	0.779
	Acetonitrile	406	539	—	0.01	—	—
	DMF	410	524	—	0.05	—	—
2b	Hexane	407	572	1.90	0.25	0.13	0.395
	Toluene	410	564	1.60	0.18	0.11	0.513
	THF	408	553	0.75	0.06	0.08	1.253
	Acetonitrile	406	541	—	0.01	—	—
	DMF	411	535	—	0.05	—	—
3a	Hexane	376, 395	458	1.99	0.80	0.40	0.100
	Toluene	379, 400	474	2.14	0.79	0.37	0.098
	THF	379, 397	485	2.72	0.87	0.32	0.048
	Acetonitrile	378, 396	525	3.70	0.80	0.22	0.054
	DMF	380, 400	533	3.78	0.77	0.20	0.061
3b	Hexane	375, 395	460	1.97	0.75	0.38	0.127
	Toluene	377, 397	475	2.09	0.80	0.38	0.096
	THF	378, 398	485	2.68	0.82	0.31	0.067
	Acetonitrile	378, 397	523	2.83	0.81	0.29	0.067
	DMF	380, 400	535	3.74	0.78	0.21	0.059

the emissions are exclusively from the CT state. Furthermore, we compared the solvent dependent intensity variation in both the series of compounds by taking **2b** and **3b** as representatives (see Fig. S8). Despite the contrasting solvatochromic photoluminescence behaviour, the spectra of the compounds showed a gradual decrease in the emission intensity in response to increased solvent polarity attributed to the stabilization of the CT state.[40,41] A detailed comparison of the quantum yield in these molecules showed significant differences among the series.

Interestingly, the compound **3** showed approximately 3 to 10 times enhancement in the quantum yield in different solvents in comparison to compound **2** (see Table 2). The molecules **2a** and **2b** showed reasonable quantum yield in nonpolar solvents hexane (0.24 and 0.25) and toluene (0.17 and 0.18), respectively, while in polar solvents the compounds showed negligible quantum yield values indicating the stabilization of the CT states. The quantum yield enhancement in molecules **3a** and **3b** in comparison to molecules **2a** and **2b** indicates the influence of ICT in determining the photoluminescence of these molecules. The compounds **2a** and **2b** in polar solvents like acetonitrile and DMF showed poor emission and therefore the lifetime was not recorded with reliability. It is noteworthy that the molecules **2a** and **2b** showed a decrease in lifetime and quantum yield on increasing the solvent polarity, while molecules **3a** and **3b** showed a constant increase in lifetime

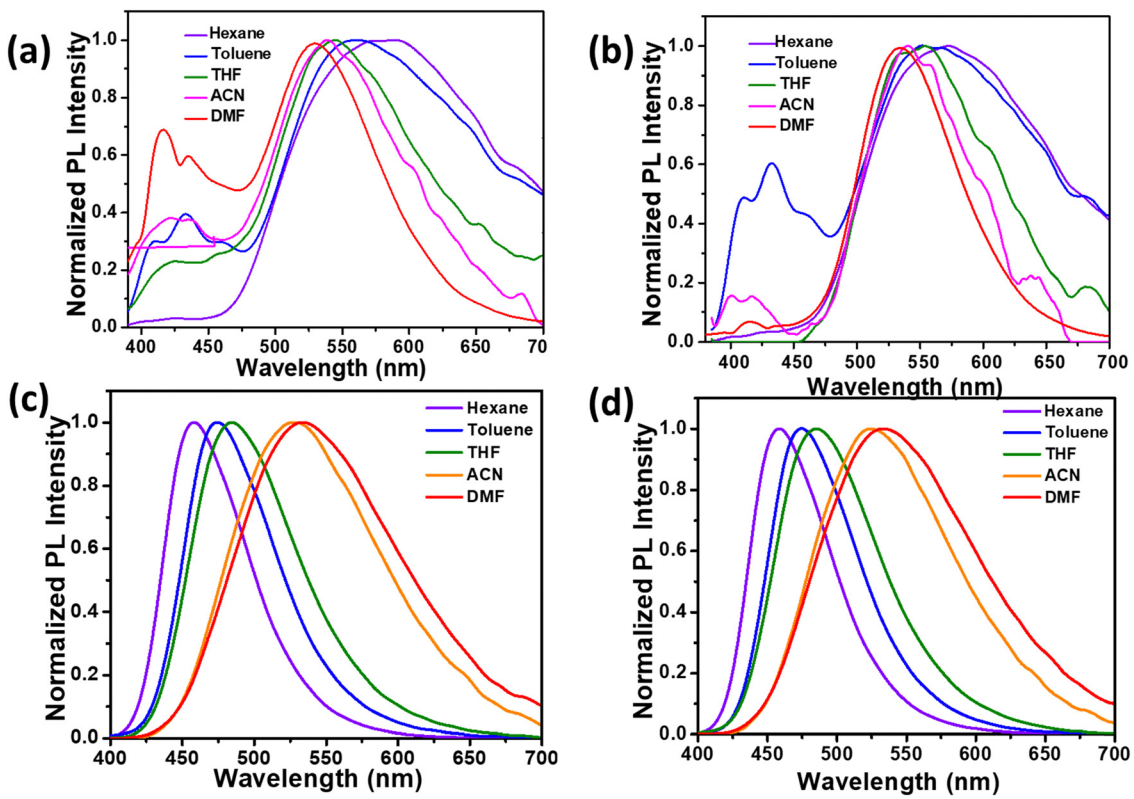

Fig. 3 Normalized emission spectra of (a) **2a**, (b) **2b**, (c) **3a**, and (d) **3b** in solvents with different polarities.

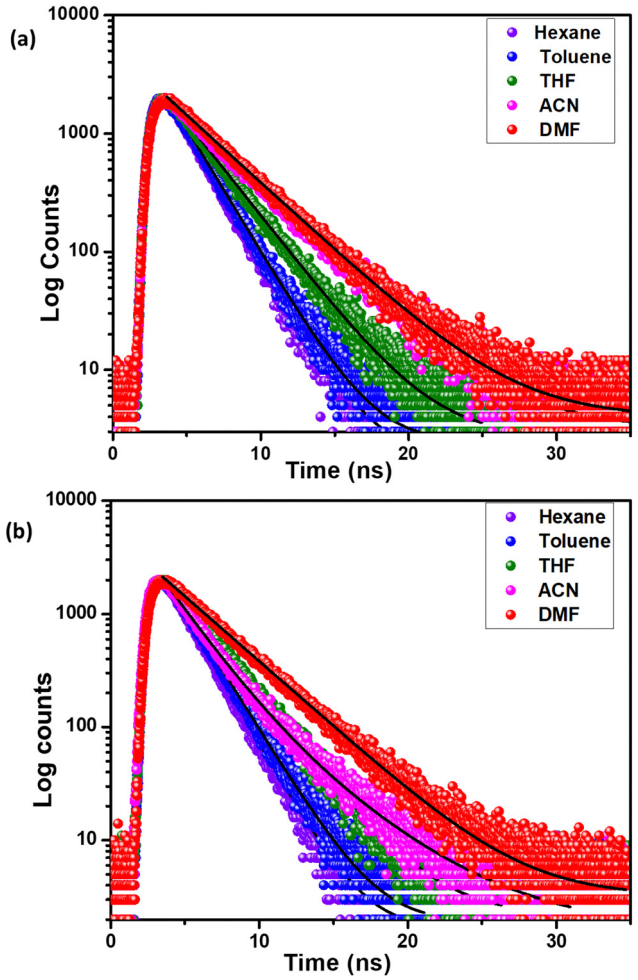

Fig. 4 Time-resolved fluorescent decay curves of (a) **3a** and (b) **3b** in different solvents.

(see Fig. 4) moving from nonpolar to polar solvents (see Table 2). In general, the radiative decay constants for all the compounds showed a diminishing trend on increasing the solvent polarity indicating the stabilization of the CT states in polar solvents.

Solid state photoluminescence

Following the distinct solution state properties of the newly synthesized compounds, the investigation focused on evaluating the solid-state luminescent behaviour by analysing their photoluminescence spectra recorded from crystalline samples. The combined spectra are presented in Fig. 5 with the corresponding photoluminescence data summarized in Table 3. The photoluminescence spectra of both compounds **2** and **3** showed significant difference in the photoluminescence maxima in response to the molecular packing and difference in conjugation. Despite the presence of a phenyl π-spacer in **3a** and **3b**, the molecules **2a** and **2b** showed maximum red shifted emission from their crystalline samples. The red-shifted emission in **2a** and **2b** could be due to the molecular aggregation in the solid state.[42]

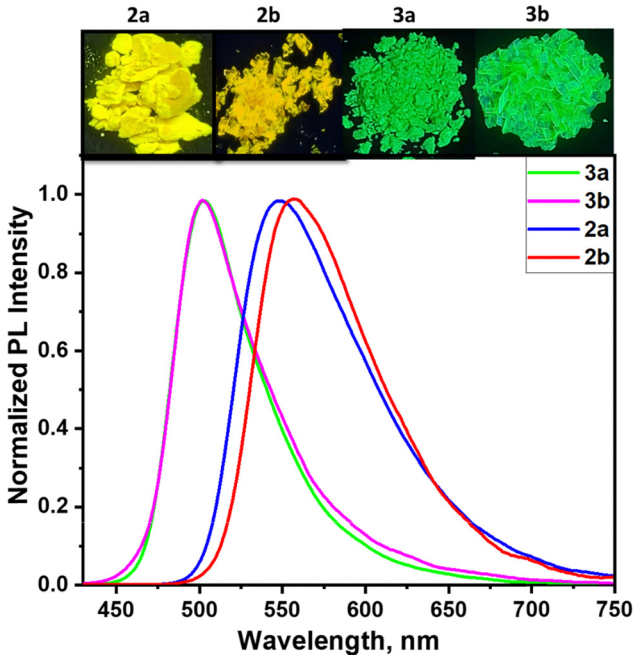

Fig. 5 Normalized solid-state emission spectra of compounds (**2a**, **2b**, **3a**, and **3b**), (λ_{ex} = 370 nm).

Table 3 Fluorescence wavelength maximum, fluorescence quantum yield and average lifetime of the **2a-3b** emitting states. Radiative and non-radiative rates (k_r, k_{nr}) were calculated using equation $k_r = \Phi_F/\tau_F$ and $\tau_F = (k_r + k_{nr})^{-1}$, respectively

Compounds		λ_{em} (nm)	Φ_F	τ_F (ns)	k_r (ns^{-1})	k_{nr} (ns^{-1})
2a	Pristine	548	0.24	3.1	0.077	0.25
	Ground	568	0.13	3.9	0.033	0.22
2b	Pristine	555	0.10	3.3	0.030	0.27
	Ground	568	0.07	3.7	0.019	0.25
3a	Pristine	503	0.31	3.9	0.079	0.18
	Ground	492	0.26	3.0	0.087	0.25
3b	Pristine	501	0.36	4.2	0.085	0.15
	Ground	490	0.31	3.7	0.087	0.19

A detailed analysis using single-crystal X-ray diffraction studies revealed the molecular arrangements in the crystals of compounds **2b** and **3b** (Fig. 6). Both **2b** and **3b** showed different levels of twist in the molecular geometry with twist angles of 81° and 69°, respectively. As seen in Fig. S9, molecule **2b** showed C–H···N and C–H···O interaction (H···N, 2.549 Å and H···O 2.472 Å) and π···π stacking interaction involving the edges of the anthracene with a distance of 3.686 Å. The intermolecular interactions in **3b** include a C–H···π (2.873 Å) interaction along with π···π (3.593 Å) stacking involving the terminal phenyl rings. In comparison, molecule **2b** showed a slipped molecular arrangement comprising a J-aggregate along the molecular long axis, while molecule **3b** resulted in a pair of aggregates slipped along the molecular short axis (Fig. 6). The molecule **3b** with non-cofacial π–π stacking gives rise to strong orbital overlap between the aromatic rings, leading to red shifted emission compared to the spectra recorded from THF

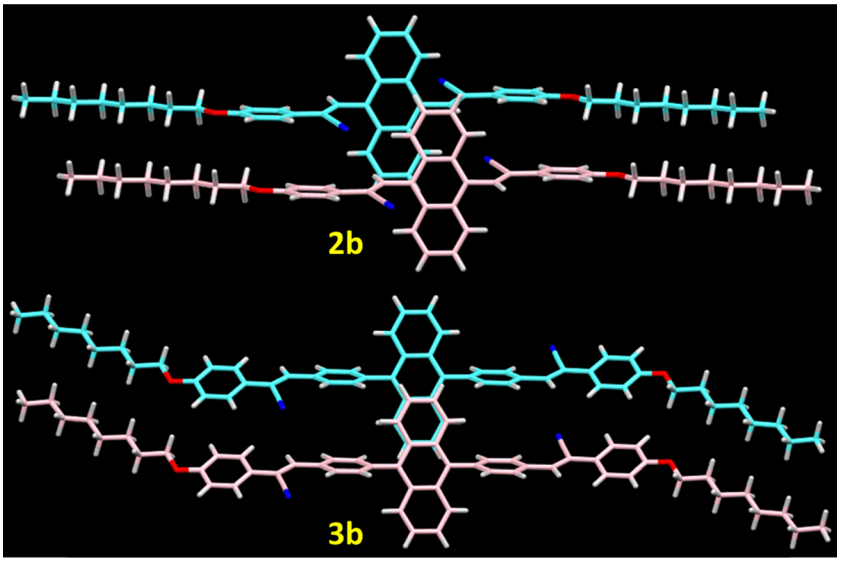

Fig. 6 Depiction of the π-interaction in the crystal structures of **2b** and **3b**.

solution. The red-shifted absorption in the solid state compared to solutions confirms J-aggregate formation in the solid state (Fig. S10). In both these molecules, the intramolecular twist restricts the cofacial π–π stacking limiting the aggregation caused quenching, where a similar observation was made in the case of 9,10-distyrylanthracene derivatives.[38,43]

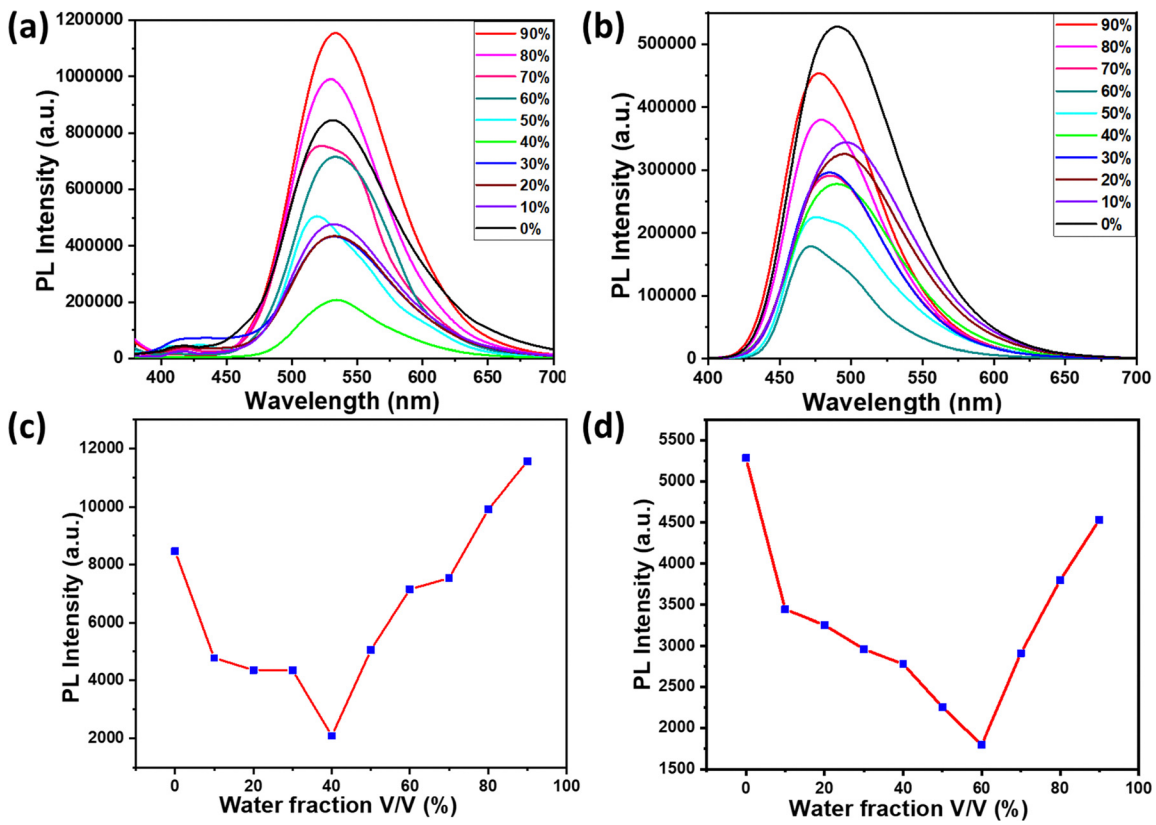

Fig. 7 Fluorescence emission spectra of the compounds (a) **2b** and (b) **3b** recorded by varying the water fraction in the THF–water mixtures with increase in the concentration of water from 0 to 90%, and (c) and (d) changes in the fluorescence intensity in response to the difference in the water fraction in the THF–water mixtures (λ_{ex} = 370 nm).

Aggregation induced emission (AIE)

The study further explored the aggregation-induced emission (AIE) in both the classes of compounds, taking **2b** and **3b** as representative molecules. The aggregation properties of the compounds were investigated by comparing the emission spectra recorded from respective THF solutions containing different water fractions. Fig. 7(a) shows the emission spectra recorded for **2a** from the THF–water mixtures. Up to 40% water fraction, the compound **2b** showed a sharp decrease in spectral intensity of the CT band. The decreased emission intensity along with blue shift on increasing the water fraction can be attributed to the stabilization of the HOMO on increasing the solvent polarity. Increasing the water fraction above 40% showed an increase in emission intensity with a slight blue shift compared to the emission spectrum recorded from THF solution, where this is clear evidence of aggregation-induced emission enhancement (AIEE) in compound **2b** (see Fig. 7(c)). The compound **3b** on increasing water fraction showed a gradual decrease in emission intensity with a red shift as represented in solvent-dependent studies. A further increase of water fraction above 60% resulted in blue-shifted emission with enhanced emission intensity (see Fig. 7(b) and (d)), where this observation can be ascribed to aggregation induced emission (AIE) in these molecules. The blue shifted emission band in **2a** on aggregation can be attributed to the formation of aggregates similar to H-aggregates, while the redshifted emission in compound **3b** is originating from aggregates similar to J-aggregates.[44–46]

Stimuli responsive emission

The newly synthesized compounds were explored for multi–stimuli responsive photoluminescence properties. All the compounds showed mechanofluorochromism (MFC) in response to applied stress. To test the possible mechanofluorochromic properties of **2a** and **2b**, the solid-state photoluminescence changes of the compounds were examined before and after grinding. The emission spectrum of **2a** exhibited a red shifted emission ($\Delta\lambda_{em}$ = 20 nm) along with an emission colour change of yellow to orange indicating an obvious MFC (see Fig. 8(a)). A subsequent fuming of the ground sample with dichloromethane vapours converted the ground sample from orange to yellow emission (see Fig. 8(b)). In contrast, the MFC studies of compounds **3a** and **3b** showed blue-shifted emission ($\Delta\lambda_{em}$ = 12 nm) compared to the pristine samples accompanied by a change in emission colour from green to cyan. The ground samples on fuming with ethyl acetate vapours resulted in recovery of emission analogous to the emission of the pristine sample (Fig. 8(c) and (d)).

In order to explore the structural origin of the stimuli-responsive emission of all the compounds, powder X-ray diffraction studies were carried out on different phases. Fig. 9(a) and (b)

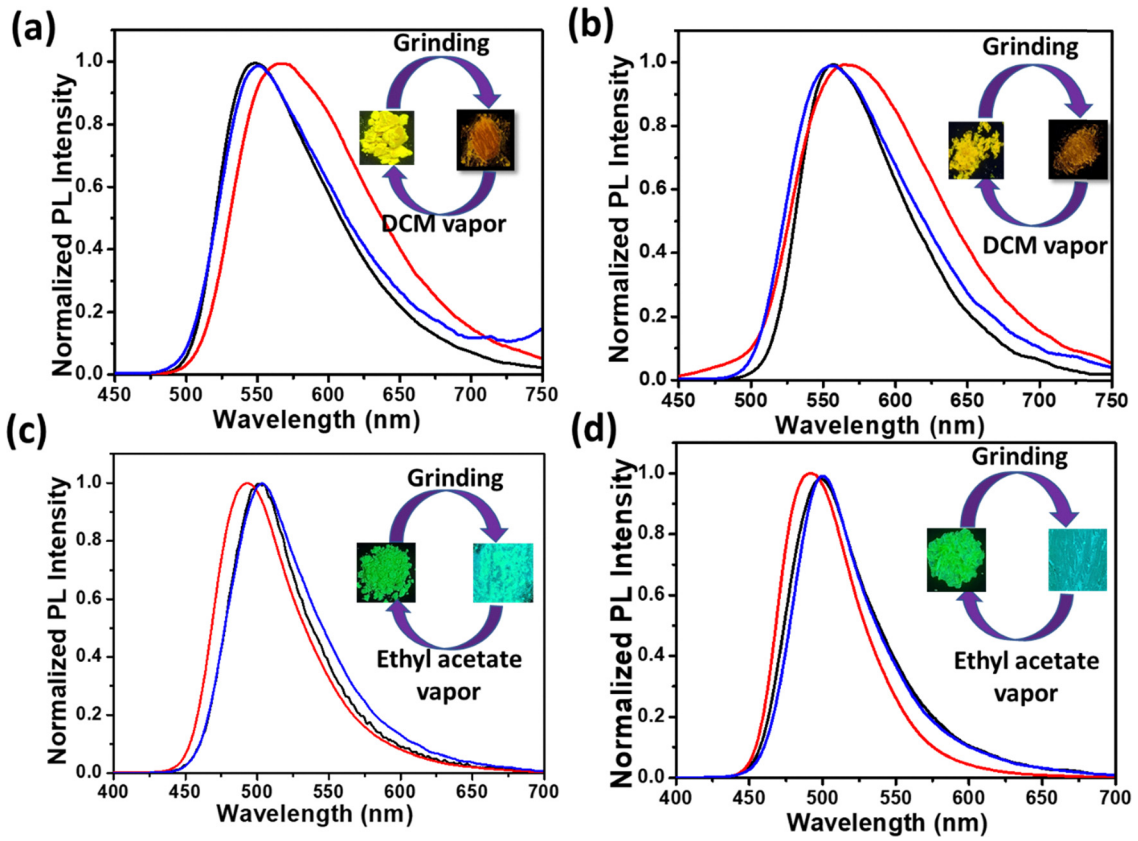

Fig. 8 Mechanochromic fluorescence spectra of (a) **2a**, (b) **2b**, (c) **3a** and (d) **3b** (λ_{ex} = 370 nm), pristine sample (black curve), ground sample (red curve), and fumed with solvent vapours (blue curve). Images taken under a UV lamp at 365 nm are shown in the inset.

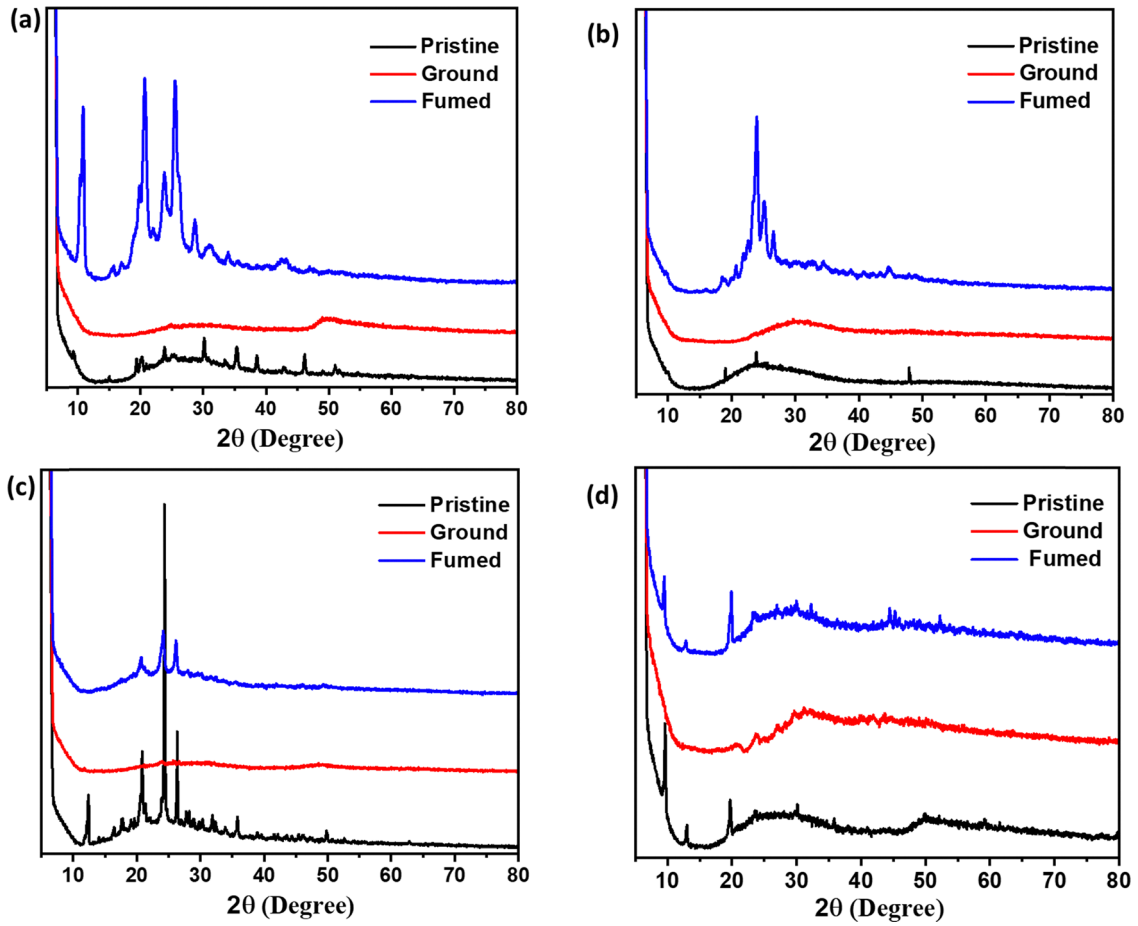

Fig. 9 PXRD patterns of compounds (a) **2a**, (b) **2b**, (c) **3a** and (d) **3b**.

show the powder X-ray diffractograms recorded from different phases of **2a** and **2b**. The pristine samples of both the compounds were crystalline in nature as indicated by the sharp peaks in the diffractogram. The compounds on grinding resulted in crystal to amorphous transitions as represented by broad featureless diffractograms in Fig. 9(a) and (b). The diffractogram recorded from the DCM fumed sample in both cases showed peaks corresponding to solvent-induced crystallisation similar to the pristine sample. Similarly, the diffractograms of **3a** and **3b** also indicate the crystalline nature of their pristine samples. The ground samples showed the formation of amorphous phase under applied stress. Interestingly, the ground samples on fuming with ethyl acetate showed recovery of the pristine phase as indicated by the sharp peaks resembling those of the pristine samples. This study demonstrates the distinct multiple stimuli-responsive nature of the two series of compounds, especially with sensitivity towards vapours of dichloromethane and ethyl acetate.

The contrasting stimuli responsive behaviour of compounds **2** and **3** is further evidenced by their distinct photophysical properties. Table 3 shows the quantum yield, fluorescence lifetime (see Fig. S11) and corresponding radiative and non-radiative decay constants for the different phases of each compound. From the tabulated data, it is evident that on grinding the photoluminescence lifetime and quantum yield decrease as a result of the introduction of new decay pathways. In all the pristine samples, the nonradiative decay is prominent as indicated by nonradiative decay constants (k_{nr}). On applying mechanical stress, the radiative decay constants for compounds **2a** and **2b** showed a substantial decrease that may be due to a more disordered arrangement of molecules in the amorphous state. In contrast, the pristine and ground phases of **3a** and **3b** showed comparable radiative and nonradiative decay constants indicating the similar molecular arrangement in the pristine and ground phases.

Quantum chemical calculations

Additional insights into the structural and photophysical properties of the synthesized compounds were gained through DFT and TD-DFT calculations, carried out at the ωB97-XD/6-311+G(d) level of theory.[47] The longer λ_{abs} values corresponding to the lowest energy transition ($S_0 \rightarrow S_1$) observed for **2**, compared to **3**, can be rationalized based on their optimized geometries and molecular electrostatic potential (MESP) analyses (Fig. 10–12).[48] The optimized geometries show good agreement with the corresponding crystal structures of

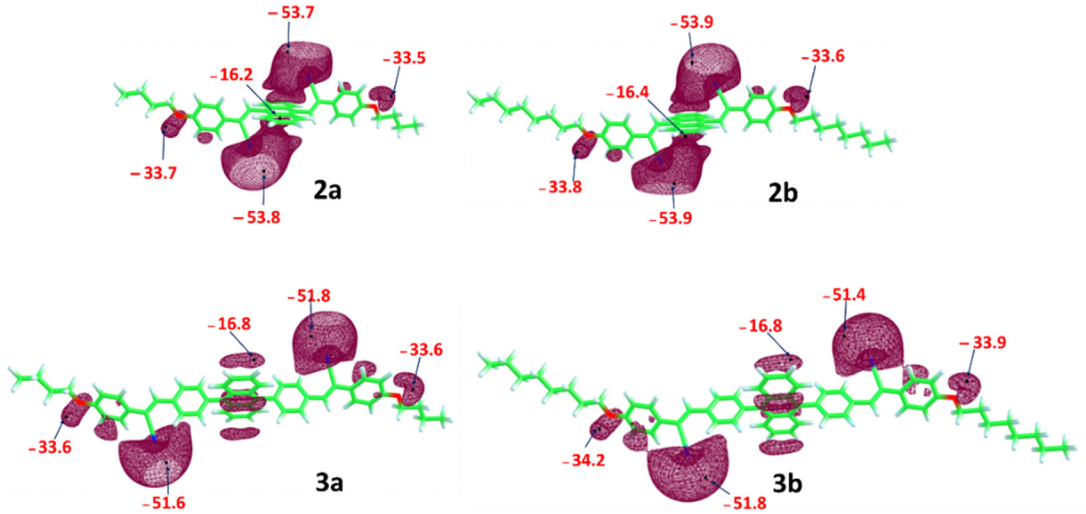

Fig. 10 MESP minimum values (V_{min} in kcal mol^{-1}) shown in the corresponding isosurface plots (at −12.5 kcal mol^{-1}).

2 and **3**. In compound **3**, the phenyl ring adopts an almost perpendicular orientation relative to the linked anthracene moiety, which disrupts the extent of π-conjugation and leads to a slightly higher HOMO–LUMO gap compared to compound **2**.

The MESP topology analysis offers a visual representation of the π-electron cloud and lone pair regions in a molecule.[49,50] The minimum electrostatic potential values (V_{min}) serve as a useful quantitative descriptor for assessing the electron density in these regions.[51,52] The MESP plot depicted in Fig. 10 showed that the V_{min} for the –CN region in compound **2** is more negative (−53.7 to −53.9 kcal mol^{-1}) than that observed in compound **3** (−51.4 to −51.8 kcal mol^{-1}). In addition, the V_{min}

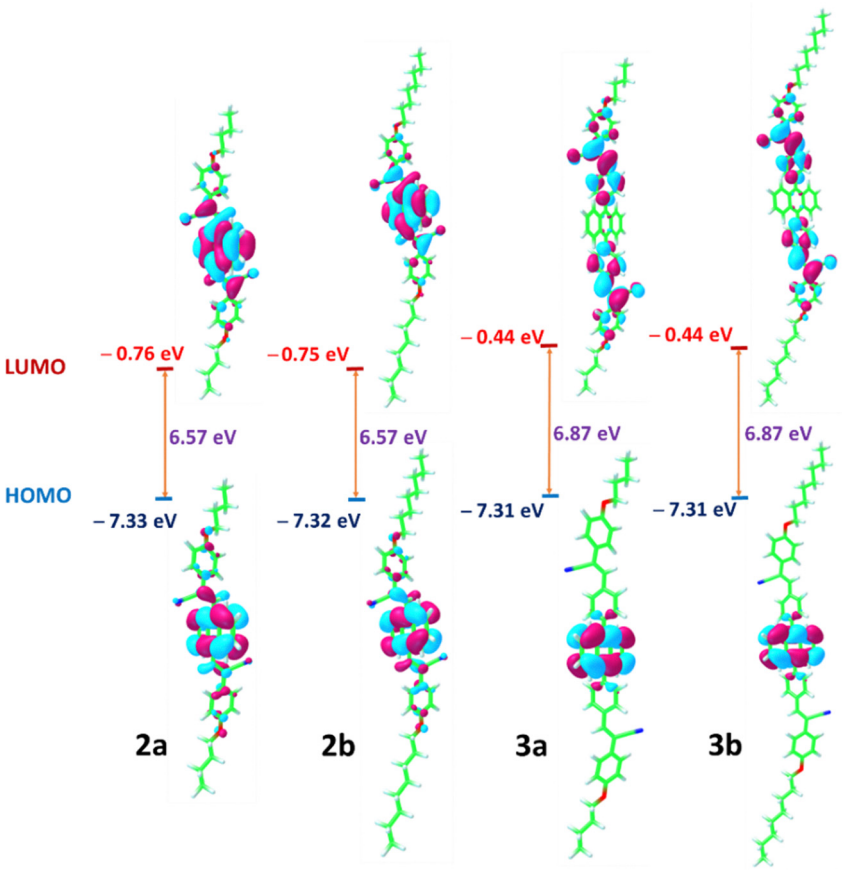

Fig. 11 The FMOs of compounds **2** and **3**.

value around the central anthracene segment in compound **3** is slightly more negative than that in compound **2**, indicating a reduced delocalization of electron density in compound **3** relative to **2**, which in turn influences the frontier molecular orbital (FMO) energy levels. The HOMO and LUMO distributions of compound **2** are localized predominantly on the central anthracene unit and cyanostilbene moieties. Instead, the HOMO of compound **3** is largely confined to the anthracene moiety, while the LUMO extends over the cyanostilbene groups, indicating the presence of ICT. The HOMO–LUMO energy gap remains essentially unchanged upon alkyl chain modification, with comparable values observed for compounds **2a** and **2b**, and a similar trend observed for compounds **3a** and **3b** (Fig. 11).

We further investigated the conformational landscapes in the ground (S_0) and first singlet excited (S_1) states of the synthesized compounds (Fig. 12). To reduce computational cost, the calculations were performed on simplified model structures by using methoxy groups for the alkyl chains. The calculations showed that both compounds **2** and **3** can exist as two primary conformers, *syn* and *anti*, based on the orientation of their terminal cyano groups. The optimized ground state geometries are referred to as S_0-Min in Fig. 12. A critical difference between the two compounds emerges from the rotational barrier between these conformers in the ground state. For compound **3**, the calculated activation barrier for the *anti* → *syn* isomerization is merely 2.92 kcal mol^{-1}. This low barrier allows for rapid interconversion at room temperature, meaning that the *syn* and *anti*-conformers, which are nearly isoenergetic (ΔG = −0.02 kcal mol^{-1}), exist as a dynamic equilibrium mixture. In stark contrast, the corresponding barrier for compound **2** is 18.44 kcal mol^{-1}. This substantial barrier effectively prevents rotation at room temperature, indicating that the *syn* and *anti*-conformers of compound **2** are

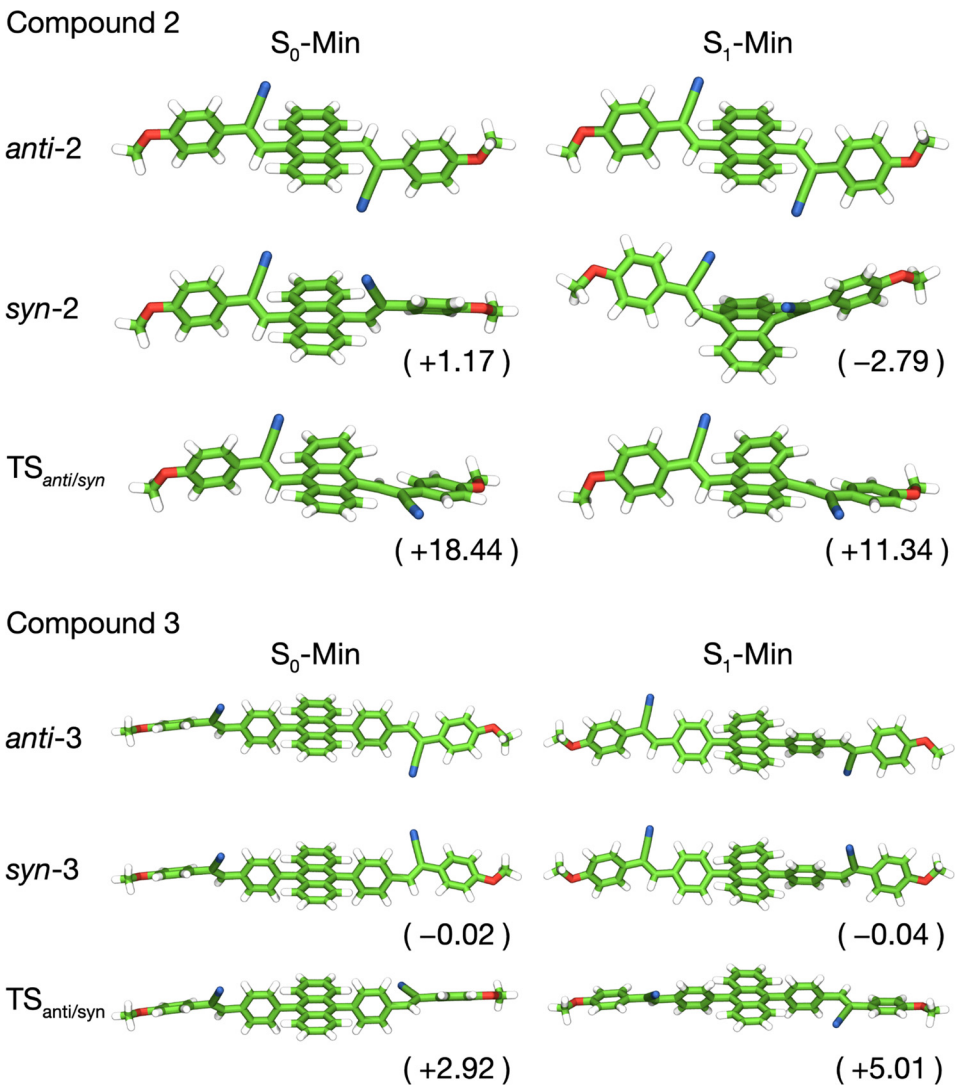

Fig. 12 Optimized geometries (ωB97-XD/6-311+G(d)) of the ground-state minima (S_0-Min), transition states (TS), and first excited-state minima (S_1-Min) for the *syn* and *anti*-conformers of compounds **2** and **3**. Relative Gibbs free energies (ΔG) in kcal mol^{-1} are shown, with the *anti*-conformer serving as the reference for each state.

configurationally locked isomers. Given that the *anti*-2 conformer is thermodynamically more stable by 1.17 kcal mol^{-1}, it is the predominant species, and photoexcitation will occur from this ground-state population.

In the S_1 state, the potential energy surface reveals a complex landscape. While compound **3** shows minimal geometric changes upon excitation, compound **2** exhibits a dramatic transformation. The *syn*-2 conformer, in particular, undergoes a profound structural change, adopting a significantly bent and non-planar geometry where the central anthracene core is distorted out of its plane. This distorted structure is the thermodynamic global minimum on the S_1 potential energy surface for compound **2**. The optimized geometries of all conformers in the S_1 state, referred to as S_1-Min, are shown in Fig. 12.

These computational findings were compared with the experimental absorption and emission spectra (Table S2). For compound **3**, which exists as a rapidly equilibrating mixture, the calculated properties of the *anti*-conformer (absorption at 357 nm, emission at 459 nm) are in good agreement with the experimental data. The calculated blue shift observed for compound **3** relative to compound **2** is consistent with the experimental results, as illustrated in the simulated absorption spectrum shown in Fig. S12. The small Stokes shift is consistent with its rigid, largely planar structure in both the S_0 and S_1 states.

For compound **2**, the calculated absorption for the dominant *anti*-2 conformer (384 nm) matches the experimental spectrum well. Our calculations predict that emission from the bent, thermodynamically stable *syn*-2 S_1-Min structure would appear at 674 nm. However, this long-wavelength emission is absent in the experimental spectrum. This absence strongly implies that the excited-state isomerization from *anti*-2 to *syn*-2 is kinetically hindered, likely by a high activation barrier on the S_1 surface, and thus does not occur. Therefore, the major CT emission band observed for compound **2** at approximately 530 nm may be attributed to emission from the locally excited state of the *anti*-2 conformer. Our calculated emission wavelength for *anti*-2 is 537 nm, which closely matches the experimental result. The large Stokes shift observed for **2** can thus be attributed to the significant geometric relaxation of the *anti*-2 conformer itself within its own S_1 potential well, without undergoing isomerization. Finally, a minor shoulder is observed in the experimental emission of **2** around 400–450 nm. This higher-energy emission is not assigned to the fully relaxed S_1 state. It may be due to emission from the initially populated, unrelaxed excited state of *anti*-2, occurring prior to complete geometric relaxation, a phenomenon consistent with hot luminescence. Further photophysical studies would be required to definitively assign this feature.

In the present investigation, the comparison of the emission properties of all the molecules rules out the effect of the alkyl chain variation in modulating the photophysical properties in the solution state. On the other hand, the presence and absence of π-spacer impart distinct photophysical properties in both solution and the solid state. In addition to the extended conjugation the π-spacer in compound **3** provides scope for intramolecular free rotation. Meanwhile, the directly linked donor–acceptor in compound **2** results in a conformationally locked state with distinct photophysical properties including negative solvatochromism. The intramolecular twist in both the molecules played a pivotal role in aggregation induced emission by preventing cofacial π-stacking and thereby aggregation caused quenching. Both the series showed unique mechanofluorochromism along with vapochromic reversibility originating from the crystal to amorphous transition and *vice versa*. With the help of the present molecular design, we demonstrated the impact of conformational restriction on the intramolecular charge transfer properties of anthracene–cyanostyrene donor acceptor systems. In line with these observations, our findings substantiate the role of spacer engineering as a powerful strategy to fine tune the photophysical behaviour of the donor–acceptor systems.

Conclusions

In summary, the present study demonstrates the markedly distinct photophysical properties of anthracene–cyanostilbene derivatives, strongly affected by the nature of the π-spacer. The newly synthesized compounds, **2** (lacking a phenyl spacer) and **3** (containing a phenyl spacer), showed pronounced differences in their fluorescence emission, lifetime, quantum yield, and external stimuli response. Notably, variation in alkyl chain length exerted minimal influence on the photophysical properties, underscoring the dominant effect of π-conjugation tuning *via* spacer modification. Crystallographic analysis revealed distinct molecular packing and intermolecular interactions that correlate with their emissive characteristics, while theoretical calculations provided insight into the electronic structures and excited-state dynamics. DFT/TD-DFT calculations were employed to investigate the electronic structures and conformational landscapes of compounds **2** and **3** in their S_0 and S_1 states. The remarkable photoluminescence properties of these compounds offer promising opportunities for further investigation towards sensing and optoelectronic applications.

Conflicts of interest

The authors declare no conflict of interest.

Data availability

The data underlying this study are available in the supplementary information (SI). The supplementary information file contains synthesis and characterization details of compounds **2a** to **3b**, crystallographic information table of **2b** and **3b**, molecular structure and details related to intermolecular interactions, and computational results (TD-DFT studies and conformational analysis), Photophysical studies of compounds **2a** to **3b**. See DOI: **https://doi.org/10.1039/d5cp03033a**.

CCDC 2417412 and 2417413 contain the supplementary crystallographic data for this paper.[53a,b]

Acknowledgements

CF acknowledges the Department of Science and Technology (DST) for funding research under Women Scientist Scheme-A (WOS-A), (DST/WOS-A/CS-126/2021). The authors thank DST-FIST, (SR/FIST/COLLEGE/2019/735) Government of India, for providing instrumentation support. We also acknowledge the University of Calicut for access to its instrumentation facilities. RT thanks RUSA-159/RUSA-SPD/2017, Govt. of India, for the research support. We gratefully acknowledge Dr Ratheesh K Vijayaraghavan (IISER- Kolkata) and Dr Chinna Ayya Swamy P. (NIT Calicut) for various photophysical measurements. The quantum chemical calculations were performed at the Research Center for Computational Science, Okazaki, Japan.

References

1 O. Ostroverkhova, Organic optoelectronic materials: mechanisms and applications, *Chem. Rev.*, 2016, **116**, 13279–13412.
2 A. C. Grimsdale, K. Leok Chan, R. E. Martin, P. G. Jokisz and A. B. Holmes, Synthesis of light-emitting conjugated polymers for applications in electroluminescent devices, *Chem. Rev.*, 2009, **109**, 897–1091.
3 M. Pope and C. E. Swenberg, *Electronic processes in organic crystals and polymers*, Oxford University Press, 1999.
4 B.-K. An, J. Gierschner and S. Y. Park, π-Conjugated cyanostilbene derivatives: A unique self-assembly motif for molecular nanostructures with enhanced emission and transport, *Acc. Chem. Res.*, 2012, **45**, 544.
5 X. Chen, D. Tan and D.-T. Yang, Multiple-boron–nitrogen (multi-BN) doped π-conjugated systems for optoelectronics, *J. Mater. Chem. C*, 2022, **10**, 13499–13532.
6 C. Femina, T. Yamagami, N. Yamamoto, R. Thomas and P. K. Sajith, Theoretical insights into aggregation-induced emission of bis(cyanostyryl)pyrrole derivatives, *Phys. Chem. Chem. Phys.*, 2025, **27**, 8478–8487.
7 W. Qin, Z. Yang, Y. Jiang, J. W. Y. Lam, G. Liang, H. S. Kwok and B. Z. Tang, Construction of efficient deep blue aggregation-induced emission luminogen from triphenylethene for nondoped organic light-emitting diodes, *Chem. Mater.*, 2015, **27**, 3892–3901.
8 S.-Y. Chen, Y.-W. Chiu and G.-S. Liou, Substituent effects of AIE-active α-cyanostilbene-containing triphenylamine derivatives on electrofluorochromic behavior, *Nanoscale*, 2019, **11**, 8597–8603.
9 Y. Sagara, M. Karman, E. Verde-Sesto, K. Matsuo, Y. Kim, N. Tamaoki and C. Weder, Rotaxanes as mechanochromic fluorescent force transducers in polymers, *J. Am. Chem. Soc.*, 2018, **140**, 1584–1587.
10 Y. Wang, X. Tan, Y.-M. Zhang, S. Zhu, I. Zhang, B. Yu, K. Wang, B. Yang, M. Li, B. Zou and S. X.-A. Zhang, Dynamic behavior of molecular switches in crystal under pressure and its reflection on tactile sensing, *J. Am. Chem. Soc.*, 2015, **137**, 931–939.
11 C. Femina, P. K. Sajith, K. Remya, R. Thomas and R. V. Solomon, Theoretical insights into the structural and optical properties of D−π–A-based cyanostilbene systems of α and β variants, *ACS Omega*, 2024, **9**, 22764–22776.
12 S. Gouthaman, A. Jayaraj, M. Sugunalakshmi, G. Sivaraman and C. A. S. P, Supramolecular self-assembly mediated aggregation-induced emission of fluorene-derived cyanostilbenes: multifunctional probes for live cell-imaging, *J. Mater. Chem. B*, 2022, **10**, 2238–2250.
13 G. Huang, X. Chang, Y. Jiang, B. Lin, B. S. Li and B. Z. Tang, Multi-stimuli responsive cyanostilbene derivatives: pH, amine vapor sensing and mechanoluminescence, *Mater. Chem. Front.*, 2020, **4**, 1720–1728.
14 Y. Zhang, H. Li, G. Zhang, X. Xu, L. Kong, X. Tao, Y. Tian and J. Yang, Aggregation-induced emission enhancement and mechanofluorochromic properties of α-cyanostilbene functionalized tetraphenyl imidazole derivatives, *J. Mater. Chem. C*, 2016, **4**, 2971–2978.
15 B. Wang and C. Wei, Stimuli-responsive fluorescence switching of cyanostilbene derivatives: ultrasensitive water, acidochromism and mechanochromism, *RSC Adv.*, 2018, **8**, 22806–22812.
16 G. Fan and D. Yan, Positional isomers of cyanostilbene: two-component molecular assembly and multiple-stimuli responsive luminescence, *Sci. Rep.*, 2014, **4**, 4933.
17 X. Wang, Z. Ding, Y. Ma, Y. Zhang, H. Shang and S. Jiang, Multi-stimuli responsive supramolecular gels based on a D–π–A structural cyanostilbene derivative with aggregation induced emission properties, *Soft Matter*, 2019, **15**, 1658–1665.
18 C. Dou, L. Han, S. Zhao, H. Zhang and Y. Wang, Multi-stimuli-responsive fluorescence switching of a donor−acceptor π-conjugated compound, *J. Phys. Chem. Lett.*, 2011, **2**, 666–670.
19 S. Rana, S. Vaidyanathan and S. Patel, Aggregation induced emission (AIE) based donor–π–acceptor fluorophores: an approach to fabricate acidochromic sensors and white light emitting diodes, *J. Mater. Chem. C*, 2024, **12**, 14148–14164.
20 G. Qian, B. Dai, M. Luo, D. Yu, J. Zhan, Z. Zhang, D. Ma and Z. Y. Wang, Band gap tunable, donor−acceptor−donor charge-transfer heteroquinoid-based chromophores: near infrared photoluminescence and electroluminescence, *Chem. Mater.*, 2008, **20**, 6208–6216.
21 B. M. Samrudhi, H. V. Barkale, D. Devadiga, N. Dey and T. N. Ahipa, Donor-acceptor-based conjugated fluorescent probes for volatile acid detection, *ChemistrySelect*, 2024, **9**, e202401790.
22 J. Zhao, C. Yao, M. U. Ali, J. Miao and H. Meng, Recent advances in high-performance organic solar cells enabled by acceptor–donor–acceptor–donor–acceptor (A–DA′D–A) type acceptors, *Mater. Chem. Front.*, 2020, **4**, 3487–3504.
23 C. Femina, M. Shanthil, P. K. Sajith and R. Thomas, Anthracene-incorporated cyanostilbene based donor–acceptor systems: intramolecular charge transfer and aggregation induced emission, *New J. Chem.*, 2023, **47**, 13810–13819.

24 Z. Jiang, H. Zhao, W. Wu, K. Chen, H. Yu, T. Wang, X. Huang, N. Wang, L. Zhou and H. Hao, Multi-stimuli responsive organic polymorphic crystals: anisotropic elasticity and plasticity, mechanochromism and photomechanical motions, *J. Mater. Chem. C*, 2023, **11**, 4375–4383.
25 Z. Huang, F. Tang, F. He, L. Kong, J. Huang, J. Yang and A. Ding, Pyrene and triphenylamine substituted cyanostyrene and cyanostilbene derivatives with dual-state emission for high-contrast mechanofluorochromism and cell imaging, *Org. Chem. Front.*, 2022, **9**, 5118–5124.
26 P. Athira, R. Nelliyulla Kappumchalil, A. R. Sachin, M. Yoosuf, R. Thomas and G. Gopakumar, Intramolecular charge transfer and stimuli-responsive emission in cholesterol-appended phenothiazine–cyanostyryl-based donor–acceptor systems, *J. Phys. Chem. A*, 2024, **128**, 3935–3946.
27 S.-Y. Chen, M.-H. Pai and G.-S. Liou, Effects of alkyl chain length and anion on the optical and electrochemical properties of AIE-active α-cyanostilbene-containing triphenylamine derivatives, *J. Mater. Chem. C*, 2020, **8**, 7454–7462.
28 N. Kumar, D. Maity, S. Som and S. Banerjee, Multi-stimuli responsive cyanostilbene assemblies in aqueous media: temporal luminescence modulation through pH-feedback network, *Small*, 2025, 2503123.
29 L. Zhu and Y. Zhao, Cyanostilbene-based intelligent organic optoelectronic materials, *J. Mater. Chem. C*, 2013, **1**, 1059–1065.
30 C. Hang, H.-W. Wu and L.-L. Zhu, π-Conjugated cyanostilbene-based optoelectric functional materials, *Chin. Chem. Lett.*, 2016, **27**, 1155–1165.
31 H. Yu, W. Wu, H. Zhao, K. Chen, S. Li, M. Tan, T. Wang, X. Huang, N. Wang and H. Hao, Cyanostyrene derivative with multi-stimuli responsive properties: Multicolor- and high-color-contrast switching in response to force, heat and light, *Dyes Pigm.*, 2023, **220**, 111727.
32 J. Xiong, K. Wang, Z. Yao, B. Zou, J. Xu and X.-H. Bu, Multi-stimuli-responsive fluorescence switching from a pyridine-functionalized tetraphenylethene AIEgen, *ACS Appl. Mater. Interfaces*, 2018, **10**, 5819–5827.
33 A. Afrin and P. Chinna Ayya Swamy, Symphony of light: AIE and MFC in carbazole-based cyanostilbenes, *J. Mater. Chem. C*, 2024, **12**, 1923–1944.
34 M. Sun, J. Liu, T. Jiang, J. Lin, M. Xu, Y. Zhao, Q. Liu, K. Chen and C. Zeng, A thiophene-substituted cyanostilbene derivative: Understanding the mechanism of its aggregation-induced emission, acidochromism and mechanochromism from the molecular level, *J. Mol. Struct.*, 2025, **1337**, 142262.
35 A. Shabashini, V. Ramar, B. Karthikeyan, M. K. Panda and G. C. Nandi, Design and synthesis of triphenylamine based cyano stilbenes for picric acid sensing and two photon absorption applications, *ChemistrySelect*, 2021, **6**, 12300–12308.
36 D. Zhang, Y. Liu, H. Gao, Q. Chang and X. Cheng, α-Cyanostilbene and fluorene based bolaamphiphiles: synthesis, self-assembly, and AIEE properties with potential as white-light emissive materials and light-emitting liquid crystal displays, *J. Mater. Chem. C*, 2020, **8**, 17474–17481.
37 H. C. Zhang, E. Q. Guo, Y. L. Zhang, P. H. Ren and W. J. Yang, Donor−acceptor-substituted anthracene-centered cruciforms: synthesis, enhanced two-photon absorptions, and spatially separated frontier molecular orbitals, *Chem. Mater.*, 2009, **21**, 5125–5135.
38 J. He, B. Xu, F. Chen, H. Xia, K. Li, L. Ye and W. Tian, Aggregation-induced emission in the crystals of 9,10-distyrylanthracene derivatives: the essential role of restricted intramolecular torsion, *J. Phys. Chem. C*, 2009, **113**, 9892.
39 M. J. Frisch, *et al.*, *Gaussian 16, Revision C.02*, Gaussian, Inc., Wallingford CT, 2016.
40 A. R. Nair, C. Raksha, R. Heera, M. Gayathri Mohan, P. Manoj and A. Sivan, D-A-D/A chalcones with tunable optical characteristics: Synthesis, photophysical, electrochemical and theoretical investigations, *J. Photochem. Photobiol., A*, 2024, **451**, 115511.
41 P. Sumsalee, P. Morgante, G. Pieters, J. Crassous, J. Autschbach and L. Favereau, Negative solvatochromism and sign inversion of circularly polarized luminescence in chiral exciplexes as a function of solvent polarity, *J. Mater. Chem. C*, 2023, **11**, 8514–8523.
42 S. Ma, S. Du, G. Pan, S. Dai, B. Xu and W. Tian, Organic molecular aggregates: From aggregation structure to emission property, *Aggregate*, 2021, **2**, e96.
43 Z. Zhao, B. He and B. Z. Tang, Aggregation-induced emission of siloles, *Chem. Sci.*, 2015, **6**, 5347–5365.
44 B. Hämisch and K. Huber, Mechanism and equilibrium thermodynamics of H- and J-aggregate formation from pseudo isocyanine chloride in water, *Soft Matter*, 2021, **17**, 8140–8152.
45 H. Piwoński, S. Nozue, H. Fujita, T. Michinobu and S. Habuchi, Organic J-aggregate nanodots with enhanced light absorption and near-unity fluorescence quantum yield, *Nano Lett.*, 2021, **21**, 2840–2847.
46 Q. He, A. Basu, H. Cha, M. Daboczi, J. Panidi, L. Tan, X. Hu, C. C. Huang, B. Ding, A. J. P. White, J.-S. Kim, J. R. Durrant, T. D. Anthopoulos and M. Heeney, Ultra-narrowband near-infrared responsive J-aggregates of fused quinoidal tetracyanoindacenodithiophene, *Adv. Mater.*, 2023, **35**, 2209800.
47 J.-D. Chai and M. Head-Gordon, Long-range corrected hybrid density functionals with damped atom–atom dispersion corrections, *Phys. Chem. Chem. Phys.*, 2008, **10**, 6615–6620.
48 J. Tomasi, Use of the electrostatic potential as a guide to understanding molecular properties, in *Chemical Applications of Atomic and Molecular Electrostatic Potentials*, ed. P. Politzer and D. G. Truhlar, Springer, US, Boston, MA, 1981, pp. 257–294.
49 S. R. Gadre, C. H. Suresh and N. Mohan, Electrostatic potential topology for probing molecular structure, bonding and reactivity, *Molecules*, 2021, **26**, 3289.
50 C. H. Suresh, G. S. Remya and P. K. Anjalikrishna, Molecular electrostatic potential analysis: A powerful tool to interpret and predict chemical reactivity, *Wiley Interdiscip. Rev.: Comput. Mol. Sci.*, 2022, **12**, e1601.
51 T. M. Ismail, N. Mohan and P. K. Sajith, Theoretical study of hydrogen bonding interactions in substituted nitroxide radicals, *New J. Chem.*, 2021, **45**, 3866–3875.

52 P. K. Anjalikrishna, S. R. Gadre and C. H. Suresh, Electrostatic potential for exploring electron delocalization in infinitenes, circulenes, and nanobelts, *J. Org. Chem.*, 2023, **88**, 4123–4133.

53 (*a*) CCDC 2417412: Experimental Crystal Structure Determination, 2025, DOI: **10.5517/ccdc.csd.cc2m4j1c**; (*b*) CCDC 2417413: Experimental Crystal Structure Determination, 2025, DOI: **10.5517/ccdc.csd.cc2m4j2d**.

